Chapter

Diluted Magnetic Semiconductor ZnO: Magnetic Ordering with Transition Metal and Rare Earth Ions

Kuldeep Chand Verma

Abstract

For advancement in future spintronics, the diluted magnetic semiconductors (DMSs) might be understood for their origin of ferromagnetic aptness. It not much clear to the ferromagnetism in DMS, that is intrinsic or via dopant clustering formation. For this, we have included a review study for the doping of transition metal and rare earth ions in ZnO. It is realized that the antiferromagnetic ordering is found in doped ZnO to achieve high-T_C ferromagnetism. X-ray diffraction and Raman spectra techniques have been used to detect the wurtzite ZnO structure and lattice defects. Since ZnO has different types of morphology formation that is generally dependent on synthesis conditions and dopant level. The band gap energy of ZnO and lattice defect formation are shown by photoluminescence technique. The room temperature ferromagnetism is described with bound magnetic polaron (BMP) model in which oxygen vacancies play a major role. However, the temperature-dependent conditions are responsible for ferromagnetic ordering. The first principle calculation is used for dopant ions in ZnO for their replacement of Zn^{2+} atoms in the wurtzite structure as well as magnetic contribution.

Keywords: ZnO ferromagnetism, lattice structure, TEM, vacancies

1. Introduction

Diluted magnetic semiconductors (DMSs) and oxides raised hopes of applications based on single elements combining the logic functionalities of semiconductors with the information storage capabilities of magnetic elements [1]. The research on DMSs is fascinating during the 1980s on II-VI semiconductors with little magnetic impurities that opened the optical and electronic phenomenon to introduce magnetic field effects [2]. The DMS required high Curie temperature, T_C, for a material. Initially, II-VI semiconductors such as CdMnTe and ZnMnSe are widely investigated as DMSs for which the valence of the cation matches with the common magnetic ions, i.e., Mn [3]. Since the hole induced ferromagnetic order in p-type InMnAs and GaMnAs, a lot of research is carried out on III-V-based DMSs that unfortunately failed to give room temperature ferromagnetism (RTFM). After that, a lot of efforts are carried out to result RTFM in III-V-based DMS, i.e., GaN, GaSb, InAs, and oxide-based DMS, ZnO, TiO_2, SnO_2, In_2O_3, etc. These DMSs are

attracting potential interest in spin-based information-processing applications. It needs high T_C for such DMSs of GaN and ZnO that may relate for their wide-band gap [4]. However, the spintronic applications like spin-valve transistors, spin light-emitting diodes, nonvolatile memory, logic devices, etc. have remarkable interest of RTFM of DMSs [5]. Among DMSs, the Mn-doped GaAs is found to be ferromagnetic with $T_C \sim 172$ K is widely investigated [5].

1.1 DMS opens new window for spintronics

Even though low transition temperatures, ferromagnetism in diluted magnetic semiconductors, DMSs is essential to explore new ideas to develop spintronic technology, which is actually the electrical manipulation of magnetism [6]. A small Mn percentage in III-V semiconductors of (In, Mn)As and (Ga, Mn)As replaces Ga or In atoms to stabilize the exchange interaction between charge carriers and localized spins. Due to low carrier concentration in these DMSs, it is possible to control a considerable portion of carriers by external electric fields using metal–insulator–semiconductor or p-n junction configuration (**Figures 1a, b**). It has a thin ferromagnetic semiconductor layer, to the extent that the field significantly alters the stability of the ferromagnetic phase and other magnetic properties. The value of T_C is controlled in a ferromagnet with the application of an electric field which was observed for metal–insulator–semiconductor configuration of (In, Mn)As thin films [8]. Later, electrical manipulation of the coercive field (H_C) is also possible for (In, Mn)As which means an applied electric field changes the magnetic anisotropy [9]. This is the exchange interaction which splits the carrier states according to the spin-orbit interaction [10].

1.2 DMS made up as a computer memory

For low-power-consumption computer memory devices, the DMSs influencing the magnetization direction to achieve magnetic data-storage and memory devices of hard disks directs with the direction of magnetization [7]. In a hard disk, the data is stored on a disk-shaped magnet in local magnetization form; to write information, a pulse of current is applied to a small electromagnet that scans the disk. In this process, an energy is wasted due to a magnetic field exists between the current and the manipulated magnetization. However, a spin-polarized current is applied directly to the magnet instead of using current to generate the magnetic field is an

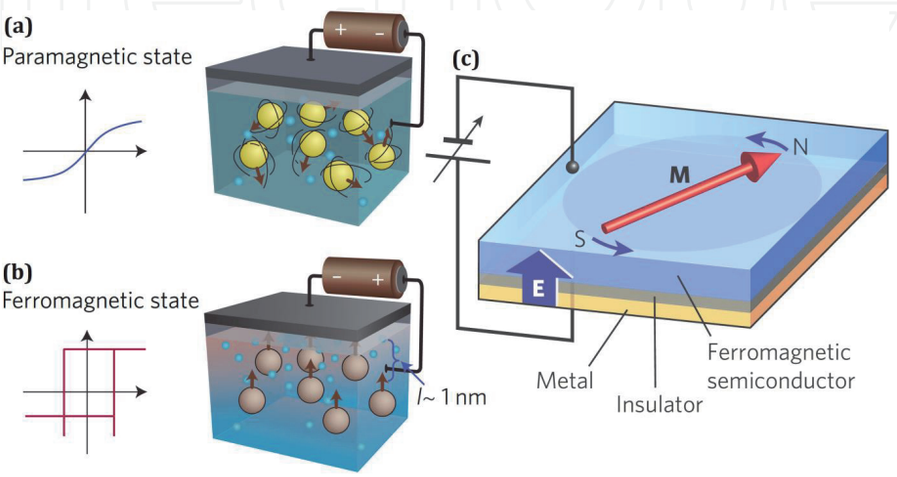

Figure 1.
(a, b) Electric control of ferromagnetism (schematic representation). (c) a spin-polarized current changes the magnetization direction, i.e., (GaMn)As (adapted from [6, 7]).

alternative way as schematized in **Figure 1c**. Such a current would exert torque on the magnetization by exchanging spin-angular momentum with it as it passes through the magnet. Exploitation of this phenomenon, called spin torque, is expected to allow the development of compact magnetic memory devices that can run on low-power consumption. In **Figure 1c**, the metal–insulator–semiconductor device involving a semiconductor—a (GaMn)As film—that has ferro magnetic properties at low temperatures [7]. The device includes a 'gate' electrode isolated electrically from the (GaMn)As film. When a negative voltage is applied to the gate electrode, carriers in the film that have positive charge (electron "holes") are attracted toward the electrode and vice versa. This property allows the density of the electron holes, and thus the magnetic anisotropy in the (GaMn)As film beneath the electrode, to be controlled electrically, resulting in a change in the magnetization direction.

1.3 Ferromagnetic origin in DMS

The researcher has initially found high T_C in doped III-V DMS, which for a long time was stuck at 110 K [1]. After that, several groups stressed out the defects—mainly Mn atoms that form interstitials rather than substituting for Ga—responsible for this limit, and T_C was raised up to 150 K. Dietl [1] proposed a Zener model to perform so many experiments on (Ga, Mn)As, which create problem with higher concentration of Mn due to the interplay between the disorder and localization, and electron–electron correlations have a very influential effect on carrier-mediated ferromagnetism at and above room temperature [11]. For example, for the Co-doped ZnO, the Co occupies the Zn sites as Co is paramagnetic and there is no ferromagnetism associated with Co, even when lots of carriers are added by Al co-doping and the temperature is very low (5 K) [12]. Moreover, the solubility of Co in ZnO is high, making it is easy to substitute Co for Zn throughout the crystal. However, by considering defect-mediated ferromagnetism, an intrinsic form of high-T_C ferromagnetism in dilute magnetic oxides with lots of defects is observed. This is because electrons associated with defects couple antiparallel to dopant spins within the orbital volume of the defect. With high T_C, the defect coupling is strong. But, it is difficult to control defects for practical applicability. To realize high-temperature ferromagnetism in DMSs, a wide-band gap ZnO is undoubtedly a major development if the ferromagnetism is unambiguously established to be intrinsic (carrier induced) [13]. Coey et al. [14] proposed that the ferromagnetic exchange is mediated by shallow donor electrons to form bound magnetic polarons that overlap to create a spin-split impurity band. It is reported that the oxygen vacancies might change the band structure of host oxides to induce ferromagnetism [15]. The formation of BMP, which includes electrons locally trapped via oxygen vacancies, with the trapped electron occupying an orbital overlapping with the d shells of transition metal (TM) neighbors, might explain the room temperature ferromagnetism (RTFM) in DMS. Within the BMP model, the greater density of oxygen vacancy yields a greater overall volume occupied by BMP, thus increasing their probability of overlapping more TM ions into the ferromagnetic domains to enhance ferromagnetism. Zhen et al. [16] used first principle calculations on Co-doped ZnO and observed the exchange coupling mechanism that accounts magnetism with oxygen vacancies.

1.4 DMS ZnO

DMS ZnO has the hexagonal wurtzite structure (direct wide-band gap, $E_g \sim 3.3$ eV at 300 K) due to its stability at room temperature and normal

atmospheric pressure. The atomic arrangement of the wurtzite structure is comprised of four zinc ions (Zn^{2+}) occupying the corner of a tetrahedral coordinate with one oxygen ion (O^{2-}) located at the center and vice versa (**Figure 2a**) [20]. The particle size, doping, and co-doping are used to induce the band gap of ZnO [17]. Dietl et al. [1] reported RTFM for DMS for which 3d ions substituted ZnO. However, the nanocrystals of pure ZnO also produce RTFM [21]. Gao et al. [22] suggested oxygen vacancies locating at the surface of ZnO nanoparticles are responsible for RTFM. It is also found that the ZnO nanoparticles had absorbed certain organic molecules to modify the electronic structure to give RTFM without any magnetic impurity ions [21].

1.4.1 Ferromagnetism of ZnO with transition metal ions

From the survey of many theoretical studies, it has been found that a slight doping of TM metal ions is likely ~5%, induce ferromagnetic ordering that observed at room temperature [21]. Venkatesan et al. [18] postulated on the basis of spin-split donor impurity-band model to observe RTFM in DMS ZnO with 5% of Sc, Ti, V, Fe, Co, or Ni, but not Cr, Mn, or Cu ions. For Cr, Mn, Cu, or Zn, no moment appreciably greater than the experimental uncertainty ($<0.1\ \mu_B$) is observed at room temperature. The basic action in a spintronic device is that the electrons are traveling from a ferromagnetic metal, through a normal metal, to a second ferromagnetic metal. When the magnetizations of the two ferromagnetic metals are in an aligned state, the resistance is low, whereas the resistance is high in the antialigned state. For the light 3d elements, the $3d^{\uparrow}$ states lie high in the $2p$(O)-4 s(Zn) gap, overlapping the donor impurity band which is spin split (**Figure 2b**). In the middle of the TM series, there is no overlap with the 3d levels and exchange is weak, but toward the end of the series, the $3d^{\downarrow}$ states overlap the impurity band, which then has the opposite spin splitting for the same occupancy. The high T_C is found whenever unoccupied 3*d* states overlap the impurity band, but not otherwise. The likely origin of the donor impurity band in ZnO films is lattice defects, such as oxygen vacancies, which have trapped between one and two electrons (F^0 centers)

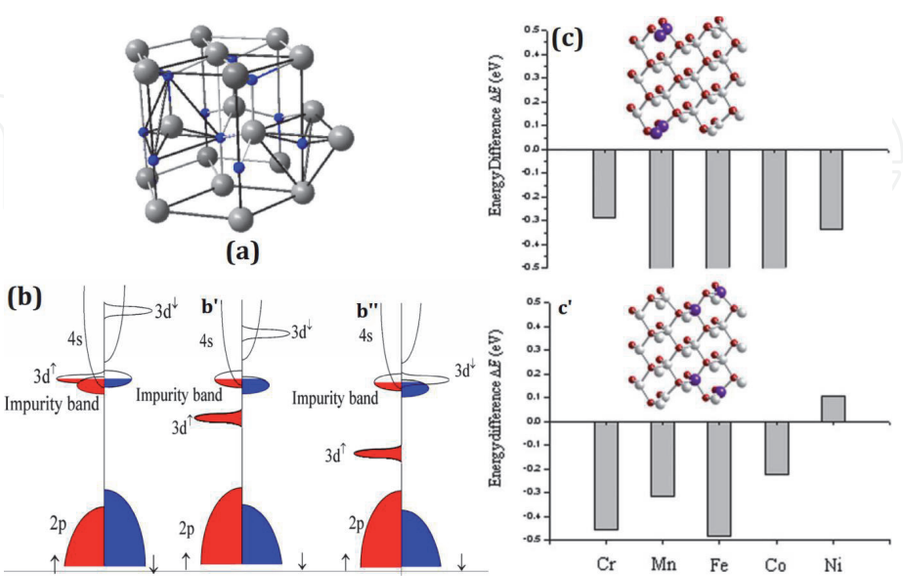

Figure 2.
(a) Hexagonal wurtzite ZnO unit cell. Density of states (schematic) of $Zn_{1-x}TM_xO$, TM = Ti (b), Mn (b′), Co (b″), for which the Fermi level lies in a spin-split donor impurity band. (c) Energy differences, $\Delta E = E_{AFM} - E_{FM}$, for $Zn_{0.857}TM_{0.143}O$ (TM = Cr, Mn, Fe, Co, and Ni) supercell; Zn(light gray spheres), O(red), and TM (purple) (adopted from [17–19]).

[18]. The electrons in the impurity band will be localized by the influence of electronic correlations and potential fluctuations associated with the dopant cations.

1.4.2 Theoretical survey on magnetism of DMS ZnO with TM = Cr, Mn, Fe, Co, and Ni ions

Wang et al. [19] reported that the Cr, Fe, Co, and Ni dopants in ZnO occupy the Zn sites and couple antiferromagnetically, while Mn exhibits no site preference and distributes uniformly in ZnO lattice. For hexagonal ZnO, the lattice constants are $a = b = 3.249$ Å and $c = 5.205$ Å [space-group $P6_3mc$ (No. 186)]. The ZnO thin film containing 28 formula units ($Zn_{28}O_{28}$) is shown in **Figure 1c** [19]. To find the magnetic coupling among TM ions, the two Zn atoms are replaced with two TM (= Cr, Fe, Co, and Ni) atoms with a dopant concentration of 14.28%. The preferred magnetic coupling between the TM atoms is determined with ferromagnetic (FM) and antiferromagnetic (AF) coupling by comparing their total energies, $\Delta E = E_{AF} - E_{FM}$. Positive ΔE means that the FM state is lower in energy than the AF state. In **Figure 1c**, when the two TM atoms are at the nearest neighbor sites on the surface, the corresponding magnetic couplings are AF. It is also reported that the total-energy difference between FM and AF states is reduced to 0.006–0.032 eV, when the distance between two TM atoms are increased to about 5.60 Å. It means that the AF interactions are short ranged in TM/ZnO. Srinivasulu et al. [23] suggested various 3d TM such as Ti, V, Cr, Mn, Fe, Co, Ni, and Cu that are also tried as dopants in ZnO to improve its optical and electrical behavior. Among these dopants, V, Cr, Mn, Co, Ni, and Cu are recognized as suitable dopants of ZnO for spintronic and magneto-optical communication devices due to their RTFM. In TM ions, the magnetization arises from partially filled 3d shells, and most of the cases since total orbital magnetic moment is zero, the magnetic moment is only due to the spin component, and hence total magnetic moment per atom is less [24]. Among TM/ZnO, Co deserved a special attention due to its highest magnetic moments (4.8 μ_B) and a positive magnetic exchange coupling constant [25]. Coey et al. [14] explained ferromagnetism in intrinsically n-type semiconductors and insulators by a model, where shallow donor electrons, created due to intrinsic defects in the semiconductors, form bound magnetic polarons with magnetic cations, which finally give rise to the ferromagnetic interaction. For BMPs, the localized spins of the dopant ion interact with the charge carriers such as oxygen vacancies, resulting in a magnetic polarization of the surrounding local moments [26]. The mediated oxygen vacancies are dependent upon dopant level and nanostructural formations.

1.4.3 Rare earth ions attributed ferromagnetism in DMS ZnO

In rare earth (RE) elements, magnetization appears due to unfilled 4f orbitals leading to higher magnetic moment per atom, though 4f electrons interacted with 5d or 6 s electrons [24], but exhibits weak exchange interaction with other RE ions, which is contrast to TM ions 3d electrons are directly interacted. The RE ion-doped ZnO has ferromagnetism that is induced by p-f hybridization via defect carriers [27]. Compared with 3d TMs, 4f RE ions have larger magnetic moments. The intrinsic defects such as oxygen vacancies play an important role on the magnetic properties of RE/ZnO. However, the exchange interaction by simultaneous doping from TM and RE ions in ZnO is 4f-5d-3d, which is antiferromagnetic when the 5d band is less than half full and the 3d band is more than half full. The first principle calculations revealed that the superexchange interaction between two magnetic Nd ions is mediated by the nonmagnetic O ions responsible for higher magnetic moment of ZnO [28]. This approach of doping RE elements with intrinsic strong

magnetic anisotropy and tailoring the coupling between dopants and defects should be a general approach toward stable ferromagnetic order in ZnO nanomaterials. Among RE ions, Sm^{3+} with five 4f electrons offers a unique possibility to induce the bifunctional properties for RTFM as well as visible luminescence in ZnO, making suitable material in spin transport properties and spin-LEDs [29].

2. Experimental methods

The DMS ZnO materials are synthesized by different methods such as thermal evaporation method [30], chemical vapor deposition [31], sol-gel spin-coating technique [32], spray pyrolysis [33], hydrothermal synthesis [34], solid state reaction [29], coprecipitation method [35], etc.

3. Results and discussion

Recently, a lot of research work has been reported on RE ion-based DMS ZnO [36]. Sun et al. [37] reported La-doped ZnO quantum dots in which luminescent behavior is greatly enhanced by introducing defects and oxygen vacancies (V_O). This is due to larger ionic size of La^{3+} in ZnO lattice that induces stress. However, Bantounas et al. [38] suggested the weak magnetic coupling in Gd/ZnO and the material remain paramagnetic at room temperature. Aravindh et al. [39] gives origin of ferromagnetism in Gd/ZnO in which oxygen vacancies play an important role. Using DFT calculation, it is analyzed that the RE Ce atoms replaced those Zn sites in the wurtzite structure, which is the nearest neighbor to TM/Fe or Co atoms [40]. The 4f electrons in Ce are tightly bound around the nucleus and shielded by $5s^2p^6d^16s^2$ electrons, leading to strong local spin. For Ce-doped TM/ZnO, the larger ratio of dopant cation to cation radius structure causes more defects, leading to a larger concentration of electrons and holes.

3.1 Wurtzite structure and defect calculation in DMS ZnO

3.1.1 X-ray diffraction of $Zn_{0.94}Fe_{0.03}Ce_{0.03}O$ and $Zn_{0.94}Co_{0.03}Ce_{0.03}O$ nanoparticles

The $Zn_{0.94}Fe_{0.03}Ce_{0.03}O$ (ZFCeO) and $Zn_{0.94}Co_{0.03}Ce_{0.03}O$ (ZCCeO) nanoparticles were synthesized by a sol-gel process [40]. **Figure 3a** shows the X-ray diffraction (XRD) results for ZFCeO and ZCCeO nanoparticles using Rietveld refinement (space group $P6_3mc$). The Rietveld refinement initiated with Zn^{2+} and O^{2-} atoms is located at (1/3, 2/3, 0) and (1/3, 2/3, z), respectively. The XRD reflections result into a hexagonal wurtzite ZnO phase. The refined lattice parameters are a(Å) = 3.259(1) and 3.262(3) and c(Å) = 5.215(3) and 5.218(2); unit cell volume, V(Å^3) = 47.9682(3) and 48.0828(2); bond length, $l_{Zn\text{-}O}$(Å) = 1.9826 and 1.9842; R_p(%) = 6.57 and 6.95; R_{wp}(%) = 9.0 and 9.8; and χ^2 = 1.97 and 2.05, respectively, for ZFCeO and ZCCeO. Lattice parameters for the hexagonal wurtzite ZnO structure is also calculated using the relation

$$\frac{1}{d^2} = \frac{4}{3}\frac{\left(h^2 + hk + k^2\right)}{a^2} + \frac{l^2}{c^2} \tag{1}$$

where a, c, h, k, l, and d have their usual meaning. The value of bond length is calculated [40]:

$$l_{Zn-O} = \sqrt{\frac{a^2}{3} + \left(\frac{1}{2} - u\right)^2 * c^2} \tag{2}$$

where

$$u = \frac{a^2}{3c^2} + 0.25 \tag{3}$$

where u is a positional parameter. The volume per unit cell for the hexagonal system is calculated using.

$$V = 0.866 \times a^2 \times c \tag{4}$$

The calculated values of the lattice parameters are a(Å) = 3.257, 3.256, 3.260, and 3.261; c(Å) = 5.207, 5.206, 5.214, and 5.217; c/a = 1.5987, 1.5988, 1.5994, and 1.5998;

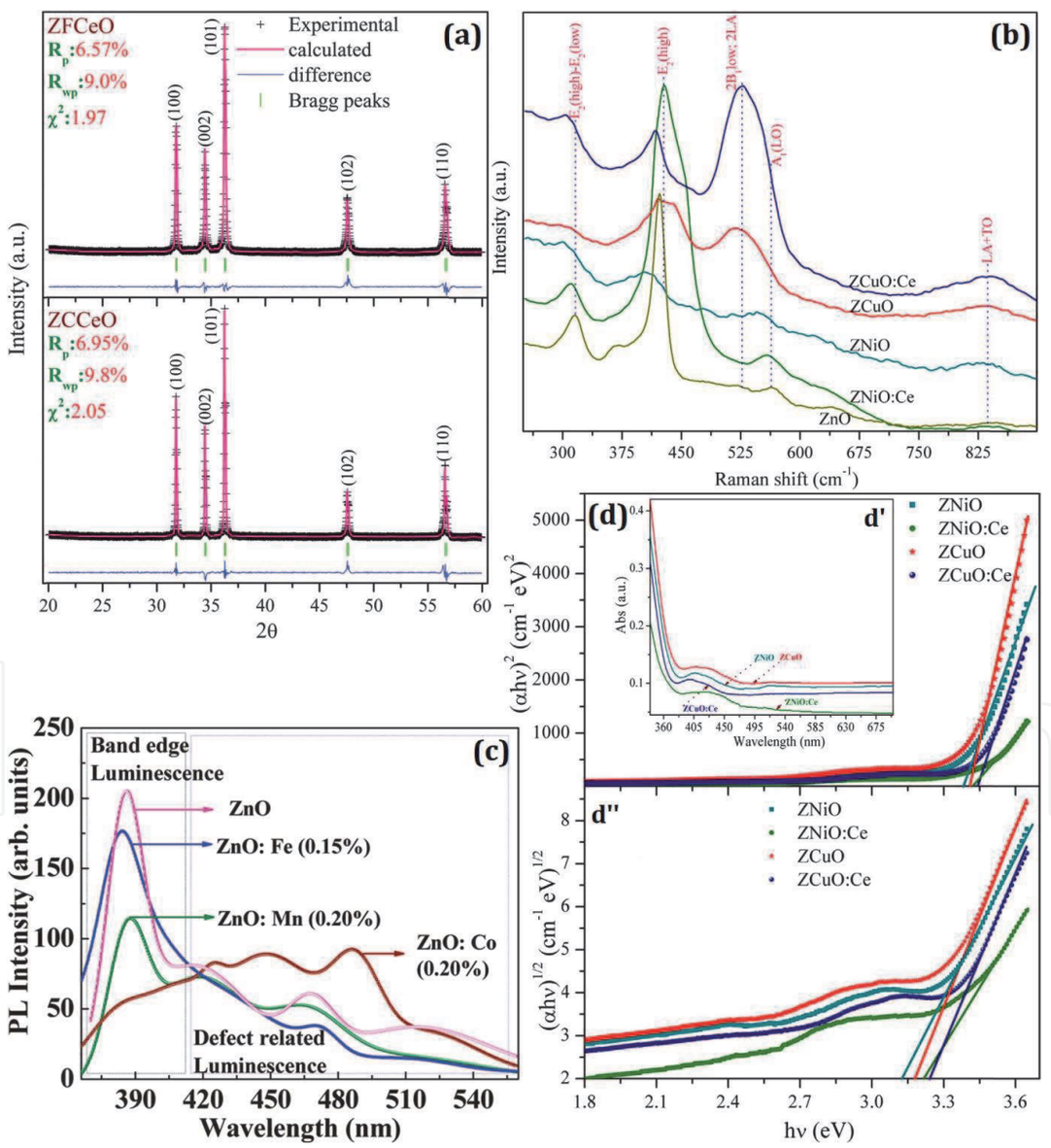

Figure 3.
(a) XRD pattern of $Zn_{0.94}Fe_{0.03}Ce_{0.03}O$ (ZFCeO) and $Zn_{0.94}Co_{0.03}Ce_{0.03}O$ (ZCCeO) nanoparticles. (b, d) Raman and UV-visible absorption (for energy band calculation) spectra of $Zn_{0.95}Ni_{0.05}O$ (ZNiO), $Zn_{0.91}Ni_{0.05}Ce_{0.04}O$ (ZNiO/Ce), $Zn_{0.95}Cu_{0.05}O$ (ZCuO), and $Zn_{0.91}Cu_{0.05}Ce_{0.04}O$ (ZCuO/Ce) nanoparticles. (c) Photoluminescence spectra for ZnO with Co, Mn, and Fe nanoparticles (adapted from [27, 40, 41]).

$l_{Zn\text{-}O}$(Å) = 1.9808, 1.9825, 1.9829, and 1.9837; and V(Å^3) = 47.834, 47.796, 47.987, and 48.044, calculated for $Zn_{0.97}Fe_{0.03}O$ (ZFO), $Zn_{0.97}Co_{0.03}O$ (ZCO), ZFCeO, and ZCCeO, respectively. The calculated values of the c/a ratio of ZFO and ZCO are slightly increased over pure ZnO (c/a = 1.598) due to the shape/size effect of the nanorods. But, it is again enhanced with RE ions due to the ionic size effect. Therefore, the observed variation in lattice parameters with doping indicated displacement of atoms in wurtzite lattice to create defects, i.e., vacancies or interstitials. It is also reported that the average size, D, of nanoparticles is 97 ± 4 nm and 106 ± 3 nm for ZFCeO and ZCCeO, respectively. The lattice defects are also evaluated with Raman and photoluminescence spectra. The zero-field cooling (ZFC) and field cooling (FC) magnetization measurement at H = 500 Oe and T = 300–5 K show AF-FM transitions. At 5 K, the measured value of M_s(emu g^{-1}) = 0.339 and 0.478 for ZFCeO and ZCCeO, respectively. For ZFCeO, the weak RTFM is formed due to the mixed valance states Fe^{2+}/Fe^{3+} via oxygen vacancies.

3.1.2 Lattice structure and defect/vacancy evaluation by Raman spectra

The $Zn_{0.95}Ni_{0.05}O$ (ZNiO), $Zn_{0.91}Ni_{0.05}Ce_{0.04}O$ (ZNiO/Ce), $Zn_{0.95}Cu_{0.05}O$ (ZCuO), and $Zn_{0.91}Cu_{0.05}Ce_{0.04}O$ (ZCuO/Ce) nanoparticles were synthesized by sol-gel process [27]. XRD pattern found wurtzite structure with lattice distortion to perform lattice defects. The average particles size is D = 27, 81, 57 and 159 nm, respectively, measured for ZNiO, ZNiO/Ce, ZCuO, and ZCuO/Ce. The Raman modes observed at room temperature for these pure Ni-, Cu-, and Ce-doped ZnO are shown in **Figure 3b**. The presence of E_2 mode in all samples indicates that the doping does not change the wurtzite phase. It is observed that Ni and Cu doping on ZnO gradually decreases the intensity of E_2(high) mode as compared with pure ZnO [22]. But, it is again strengthen with Ce co-doping. This type of change in E_2(high) mode with dopant ions might induce structural defects and local lattice distortions of wurtzite lattice [32]. The E_2(high)-E_2(low) modes indicate oxygen defects or vacancy formation. The peak position of E_2(high) mode also changes with Ni, Cu, and Ce doping that is ascribed with the change in the level of oxygen vacancies [33]. The magnetic results also reported low temperature ZFC/FC magnetic measurement that show AF-FM ordering and the doping of Ce ions results to high T_c. At 300 K, the values of M_s(emu g^{-1}) = 0.073, 0.085, 0.053, and 0.132, and at 10 K M_s(emu g^{-1}) = 0.096, 0.198, 0.136, and 0.251, respectively, for ZNiO, ZNiO/Ce, ZCuO, and ZCuO/Ce. The enhancement in the oxygen vacancies and ferromagnetism with Ce doping might depend on mixed valence state Ce^{3+}/Ce^{4+} ions.

3.1.3 Photoluminescence spectra for Fe-, Co-, and Mn-doped ZnO nanoparticles

The photoluminescence spectra for Fe (0.15%)-, Co (0.20%)-, and Mn (0.20%)-doped ZnO nanoparticles are given in **Figure 3c** [41]. Pure ZnO nanoparticles show emission maxima at 385 nm along with blue (424 nm, 468 nm) and green (521 nm) luminescence. Transitions from Zn interstitials to valence band are attributed with blue emission (424 nm). Oxygen vacancies are related with blue (468 nm) and green emission (521 nm). The green emission is understood to be due to the recombination of electrons in singly occupied oxygen vacancies with photoexcited holes in the valence band. The blue emission is caused by two defect levels, either transition from Zn_i to the valance band or transition from bottom of the conduction band to the interstitial O(O_i).

3.1.4 UV-Visible absorption spectra and Tauc plot

Figure 3d′ shows UV-visible absorption spectra measured at room temperature for Ni-, Cu-, and Ce-substituted ZnO nanoparticles. The absorption peaks are observed corresponding to violet emission, i.e., ZNiO (409 and 426 nm), ZNiO/Ce (433 nm), ZCuO (407 and 427 nm), and ZCuO/Ce (401 and 429 nm). In order to evaluate the effect of dopant on Ni, Cu, Ce, on ZnO, the energy band gap, Eg, is calculated using the Tauc relation [27] used for a direct transition using: $(\alpha h\nu)^2 = K(h\nu - E_g)$; and for an indirect transition:$(\alpha h\nu)^{1/2} = K(h\nu - E_g)$. The symbols in these equations have their usual meanings. In **Figure 3d**, the value of direct band energy, E_g(direct) = 3.38, 3.42, 3.41, and 3.44 eV, and from **Figure 7d″**, the indirect energy band gap, E_g(indirect) = 3.13, 3.21, 3.19 and 3.24 eV, respectively measured, for ZNiO, ZNiO/Ce, ZCuO, and ZCuO/Ce. These values of E_g show small variation with bulk sample of pure ZnO [27]. However, a significant change in E_g value from direct and indirect measurement clearly indicates that some of the defect states are present in the forbidden region.

3.2 Microstructural study of DMS ZnO

3.2.1 SEM image of Mn-doped ZnO nanowires

The ZnO nanowires were synthesized by a thermal evaporation method with 1 atom % Mn doping [44]. **Figure 4a** is a SEM image of Mn/ZnO nanowires of several micrometer lengths and 70 nm diameters. The reported work given T_C to be 437 K

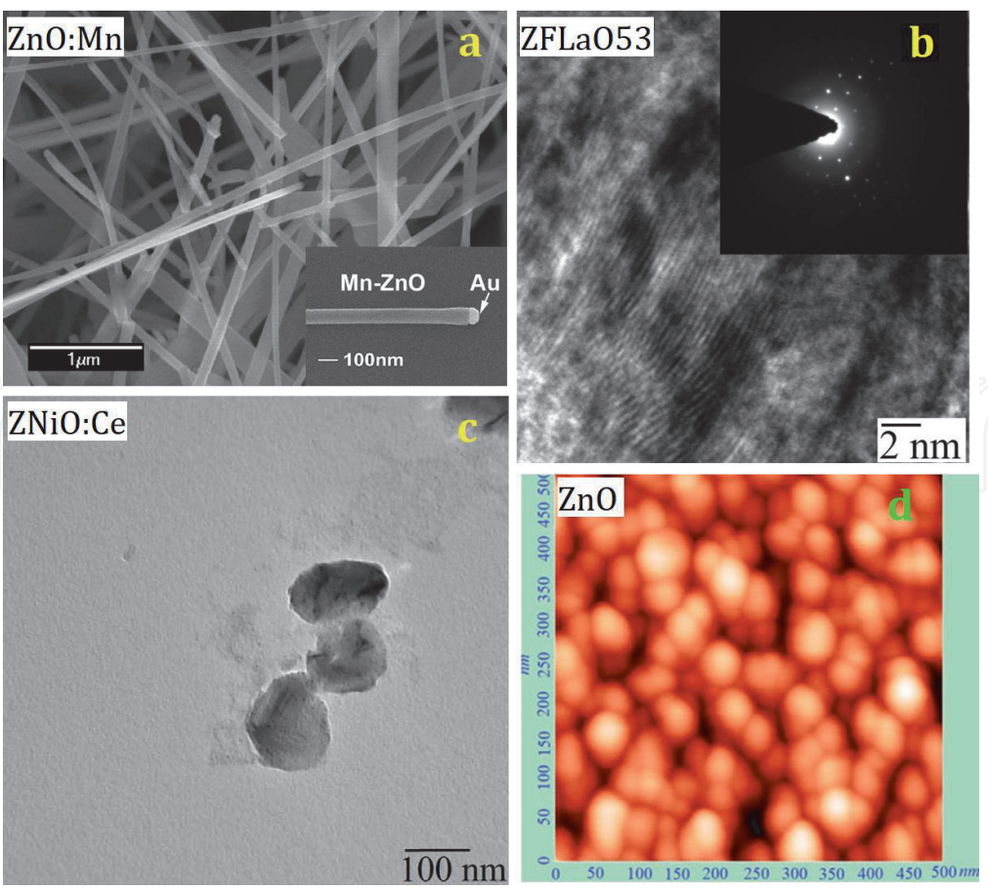

Figure 4.
(a) Scanning electron microscopy (SEM) pattern for ZnO/Mn nanowires. (b) HRTEM for $Zn_{0.92}Fe_{0.05}La_{0.03}O$ nanoparticles. (c) TEM pattern for $Zn_{0.91}Ni_{0.05}Ce_{0.04}O$ nanoparticles. (d) AFM pattern for pure ZnO (adapted from [21, 27, 44, 45]).

from SQUID measurements. The difference of ΔMR is up to 2.5% as the gate voltage changes from −40 to +40 V at T = 1.9 K, which suggests the electric field control of ferromagnetism for realizing spin logic devices.

3.2.2 HRTEM of $Zn_{0.92}Fe_{0.05}La_{0.03}O$ nanoparticles

DMSs $Zn_{0.92}Fe_{0.05}La_{0.03}O$ (ZFLaO53) nanoparticles were synthesized by sol-gel process [21]. The value of nanoparticles size is 99 nm. The lattice spacing is calculated from high-resolution transmission electron microscopy (HRTEM) images (**Figure 4b**), which show that the distorted lattice has an enhanced interplanar spacing d [(101) planes] of ∼ 0.247 nm. It is also observed from HRTEM that some fractions within the lattice fringes are formed. This may due to some ferromagnetic clustered growth by dopants in Zn^{2+} lattice. The high crystallinity of the particles is evident from the selected area electron diffraction.

3.2.3 TEM of $Zn_{0.91}Ni_{0.05}Ce_{0.04}O$ nanoparticles

The $Zn_{0.91}Ni_{0.05}Ce_{0.04}O$ (ZNiO/Ce) nanoparticles were synthesized by a sol-gel process [27]. **Figure 4c** shows their TEM image with an average size of nanoparticles of 81 nm.

3.2.4 Atomic force microscopy (AFM) of pure ZnO

The ZnO thin film is prepared by a sol–gel MOD method [45] with the average size of nanoparticles of 40 nm (**Figure 4d**).

3.3 First principle calculation for DMS ZnO with TM and RE ions

3.3.1 Magnetic behavior of $Zn_{1-x}TM_xO$ (T = Cr, Mn, Fe, Co, and Ni)

The magnetic properties of $Zn_{1-x}TM_xO$ (T = Cr, Mn, Fe, Co, and Ni) thin films are investigated using first principle calculations on the basis of DFT theory within the generalized gradient approximation (GGA) [19]. Self-consistency is achieved by allowing the total energy to converge within 1 meV because of very small-energy difference expected between the FM and AF states. **Figure $5a_1$–a_4** shows that TM 3d levels dominate the density of states (DOS) at the Fermi energy and overlap with O 2p states. This indicates that there is a strong interaction between TM and the neighboring O atoms, which results into opposite magnetic moments of O atoms. The contribution to the moment coming from TM 3d orbitals is $2.859\mu_B$, $3.930\mu_B$, $3.189\mu_B$, $2.095\mu_B$, and $1.015\mu_B$ for TM = Mn, Cr, Fe, Co, and Ni, respectively. In the ground state configuration, the AF state is found to be lower in energy by −0.094, −0.601, −0.832, −0.098, and − 0.102 eV than the FM state for $Zn_{0.929}TM_{0.071}O$ with TM = Cr, Mn, Fe, Co, and Ni, respectively.

3.3.2 Densities of states of Gd ions in ZnO

Figure 5b shows the first-principle calculation for $Zn_{46}O_{48}Gd_2$ and $Zn_{46}O_{47}Gd_2$ nanowires with and without oxygen vacancies, V_O [39]. The spin-up and spin-down DOSs of doped nanowire are significantly different from that of the pristine nanowire. The majority Gd f states (spin-up) that are located well below the valence band maximum are fully occupied. However, the minority unoccupied Gd f states are localized in the vicinity of the Fermi level. The Gd d states in the conduction band overlap with the Gd f states. The hybridization of Gd f states with the states of

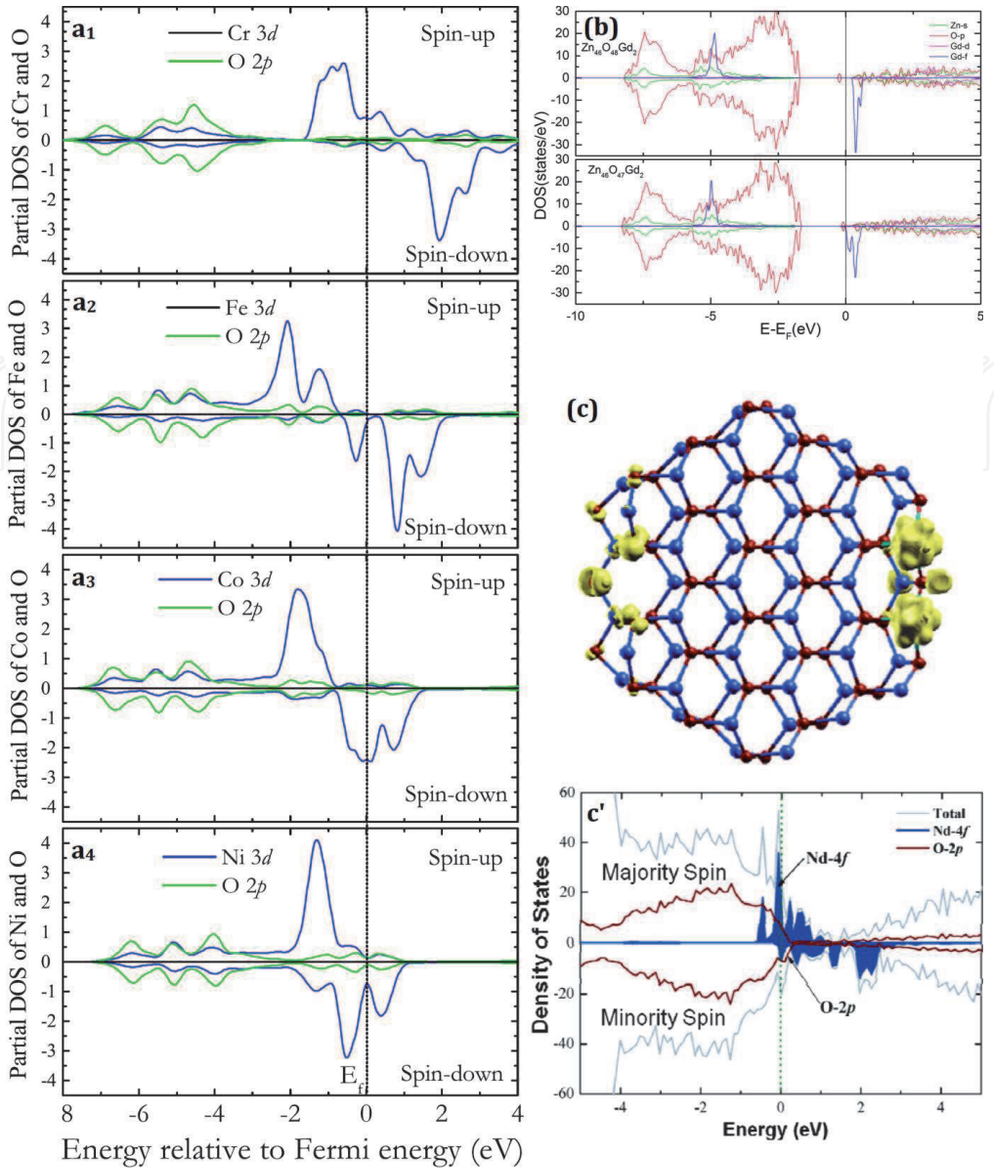

Figure 5.
(a_1–a_4) partial spin DOS of TM 3d and O 2p in $Zn_{24}TM_4O_{28}$ supercell. (b) DOS of $Zn_{46}O_{48}Gd_2$ and $Zn_{46}O_{47}Gd_2$ supercell. (c, c′) Total and projected DOS of $Zn_{51}V_{Zn}O_{54}Nd_2$ nanowire. Fermi level spin-density isosurface (green dotted), Zn(blue), O(red), and Nd(green spheres) (adapted from [19, 28, 39]).

the host material occurs at the Fermi level. By introducing oxygen vacancies, the Gd f state near the Fermi energy becomes partially occupied by donor electrons. Consequently, the carrier concentration around V_O is increased, which mediates the interaction between the s (mostly from Zn) and f electrons. This is evident from the DOS, as the s-f coupling is more prominent than p-f and f-f couplings. For such case, the carrier involved long-range ferromagnetic order to determine the exchange interactions in DMS ZnO. Moreover for these Gd-doped ZnO, oxygen vacancies donate two electrons to the system, mediating the ferromagnetic exchange, and hence, the s-f coupling is more prominent than other mechanisms.

3.3.3 Giant anisotropy in Nd/ZnO nanowire

In **Figure 5c**, the origin of the giant magnetic moment and anisotropy at atomic level is performed by spin-polarized DFT calculations on $Zn_{52}O_{54}Nd_2$ nanowire model using spin density ($\Delta\rho = \rho\uparrow - \rho\downarrow$) and the projection of DOS onto the O-2p and Nd-4f orbitals [28]. The total magnetic moment is high as 6 μ_B calculated from

supercell and 3 μ_B per unit cell, and the two Nd atoms are ferromagnetically coupled. It is found that the magnetism mainly comes from the 4f electrons of Nd ions with the local spin moment of ~3 μ_B, and both Zn and O atoms have nearly zero spin contribution. Moreover, significant hybridization is observed between Nd 4f and O 2p orbitals, which leads to the superexchange interaction between two magnetic Nd ions mediated by the nonmagnetic O ions. Both O and Zn vacancies are considered, and it is found that V_{Zn} can enhance the magnetism of about 1 μ_B as compared with defect-free system. This enhanced magnetism mainly comes from the unsaturated 2p orbitals of the surrounding O atoms.

3.4 DMS ZnO with TM = Cr and Mn ions

3.4.1 RTFM in $Zn_{0.94}Cr_{0.06}O$ nanorods

The $Zn_{0.94}Cr_{0.06}O$ nanorods were synthesized by a radio frequency magnetron sputtering deposition technique at different substrate temperatures [46]. The Cr K-edge X-ray absorption near-edge structure and X-ray photoelectron spectroscopy (XPS) results revealed that the Cr^{3+} ions are located at the substitutional Zn sites. The magnetization versus the magnetic field (M-H) loops of $Zn_{0.94}Cr_{0.06}O$ nanorods measured at room temperature is shown in **Figure 6a**. The moment per Cr atom increases with the increasing substrate temperature. The sample prepared at room temperature has a net moment of 0.76 μ_B/Cr. With increasing substrate temperature to 650°C, the value of magnetic moment shows a remarkable increase to 1.16 μ_B/Cr. The coercive field, H_c, of $Zn_{0.94}Cr_{0.06}O$ nanorod grown at room temperatures, 300, 500, and 650°C, are around 104, 42, 53, and 82 Oe, respectively.

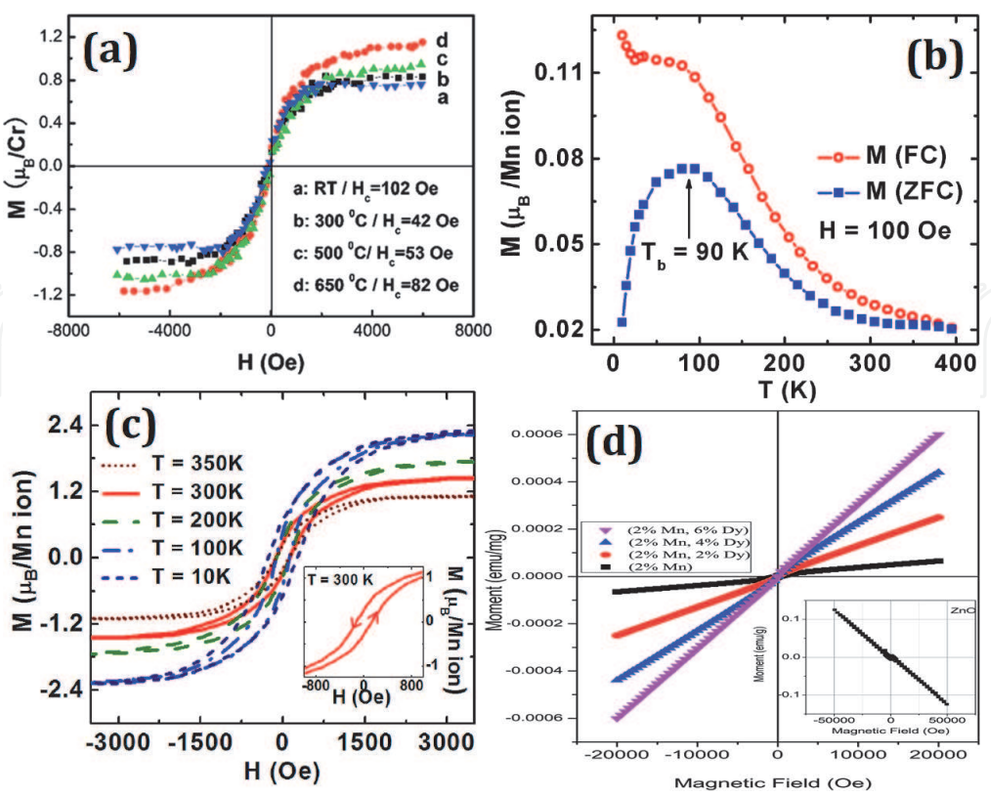

Figure 6.
(a) M-H hysteresis of $Zn_{0.94}Cr_{0.06}O$ nanorods. SQUID measurements: Magnetic moment (b) with temperature (c) with applied field, for ZnO/Mn nanowires. (d) M-H plots for ZnO/(Mn, Dy) nanoparticles (adapted from [24, 44, 46]).

3.4.2 Temperature-dependent magnetization in Mn(1 atom%)/ZnO nanowires

The Mn(1 atom%)-doped ZnO nanowires were synthesized by a gas phase surface diffusion process using MBE system [44]. **Figure 6c** shows the M-H hysteresis loops measured at T = 10, 100, 200, 300, and 350 K for an assembly of Mn-doped ZnO nanowires. The extracted M_s is 2.2 μ_B/Mn ion at 10 K and reduces to 1.4 μ_B/Mn ion at 300 K. Both values are smaller than the theoretical value of 5 μ_B/Mn ion of Mn^{2+} state [1]. The temperature-dependent magnetization (**Figure 6b**) via ZFC and FC at H = 100 Oe shows a typical FM behavior while no intersection is observed in the temperature region of 10–400 K, which reaffirms that T_c is higher than 400 K. However, these FC/ZFC curves show the blocking temperature at T_b = 90 K. The existence of the blocking temperature may result from intrinsic defects, such as oxygen vacancies [47], which contribute weak intrinsic ferromagnetism. The bifurcation begins to increase as the temperature goes below 100 K, and the effect of the external magnetic field starts to overcome the thermal fluctuation and dominate the overall magnetization when the temperature is lower than 100 K.

3.4.3 Magnetism with simultaneous doping from Mn and Dy in DMS ZnO

Figure 6d shows the magnetic results at room temperature with simultaneous doping of Mn and Dy in ZnO nanoparticles prepared by sol–gel process (Mn = 0 and 2% and Dy = 0, 2, 4, and 6%) [24]. The M-H results show that as doping concentration of Dy is increased, magnetic behavior changes from weak ferromagnetic/superparamagnetic to ferromagnetic states. The observed magnetic behavior is linked with oxygen vacancies as determined with EXAFS and PL measurements. The oxygen vacancy-mediated exchange interaction between the Dy^{3+} ions is due to the formation of BMPs.

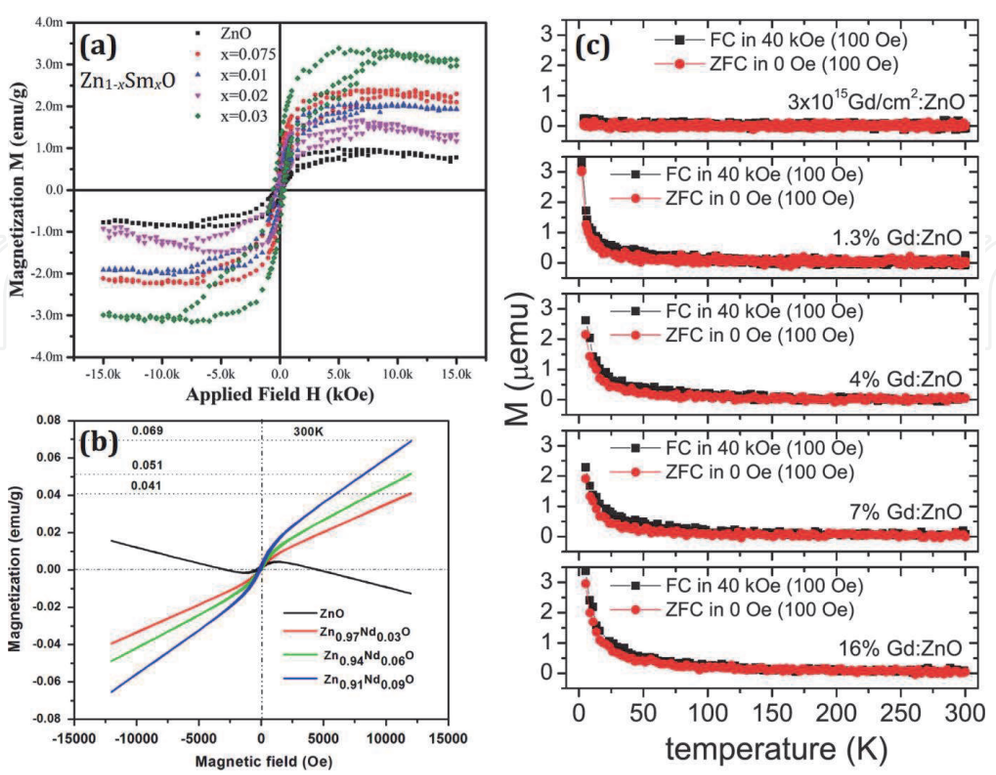

Figure 7.
(a) M-H hysteresis for ZnO/Sm nanoparticles. (b) M-H hysteresis for ZnO/Nd. (c) SQUID M(T) behavior for ZnO/Gd (adopted from [29, 42, 43]).

3.5 DMS ZnO with RE ions

3.5.1 RTFM in Sm/ZnO

The RTFM is enhanced with Sm doping into ZnO is given by M-H hysteresis at room temperature (**Figure 7a**) [29]. It infers that ferromagnetism is intrinsic and formed due to the percolation of BMPs. These BMPs are made up with magnetic cations and defect carrier. A very weak ferromagnetism is observed in pristine ZnO, which is the effect of Zn_i and/or oxygen vacancy defects rather Zn vacancies (V_{Zn}). Because the formation energy of V_{Zn} is too high, it is not preferably formed in ZnO [48].

3.5.2 RTFM in Nd/ZnO

The pure and Nd-doped ZnO nanoparticles were synthesized by the coprecipitation method, and the magnetic results are shown by M-H hysteresis (**Figure 7b**) [42]. All the M-H hysteresis exhibited weak ferromagnetism at room temperature. However, the magnetization increases with increasing Nd^{3+} concentration. The value of saturation magnetization, M_S, is (emu g^{-1}) = 0.041, 0.051, and 0.069, respectively, for $Zn_{0.97}Nd_{0.03}O$, $Zn_{0.94}Nd_{0.06}O$, and $Zn_{0.91}Nd_{0.09}O$. The concentration of oxygen vacancies has a major role in mediating FM exchange interaction among Nd^{3+} ions. It is revealed that O vacancies and Zn interstitials are generated with an increase in Nd^{3+} doping to induce long-range ferromagnetism consistent with the BMP model. Moreover, the s-f coupling between the RE ions (f) and the ZnO host(s) states contributed ferromagnetism of DMSs [14]. The coercivity is also increased with Nd^{3+} concentration.

3.5.3 Temperature-dependent magnetization in Gd/ZnO

Ney et al. [43] reported that for small doping concentrations (1.3% Gd), a large fraction of the Gd atoms is substitutional on Zn lattice sites within wurtzite structure. The magnetic behavior is purely paramagnetic with magnetic moment 7 μ_B/Gd. **Figure 7c** shows the temperature-dependent magnetization from SQUID measurement for Gd-doped ZnO with different Gd concentrations using FC and ZFC conditions [43]. No separation between FC and ZFC magnetization occurs at any temperature, which provides no evidence for ferromagnetic-like behavior. Therefore, all samples have to be considered as paramagnetic. This is in contrast to previous work, where signs of ferromagnetic-like behavior are found for Gd-doped ZnO [49].

3.6 DMS ZnO with Fe and La ions

3.6.1 RTFM in Fe/ZnO nanorods

The $Zn_{1-x}Fe_xO$ (ZFO) [x = 0.01 (ZFO1), 0.03 (ZFO3), and 0.05 (ZFO5)] nanorods were synthesized by a sol-gel process [50]. The XRD pattern revealed the hexagonal wurtzite structure with Fe doping. TEM images show nanorod formation with an average diameter, D(nm) = 10, 48, 14, and 12, and length, L(nm) = 23, 113, 50, and 30, respectively, for ZnO, ZFO1, ZFO3, and ZFO5. **Figure 8a** shows M-H hysteresis for pure and Fe-doped ZnO at room temperature. Pure ZnO exhibits diamagnetic behavior, whereas ZFO samples display superferromagnetic behavior. The values of are M_s(emu g^{-1}) = 0.233, 0.459, and 0.328, respectively, measured for ZFO1, ZFO3, and ZFO5 nanorods. The variations in M_S values depend on factors

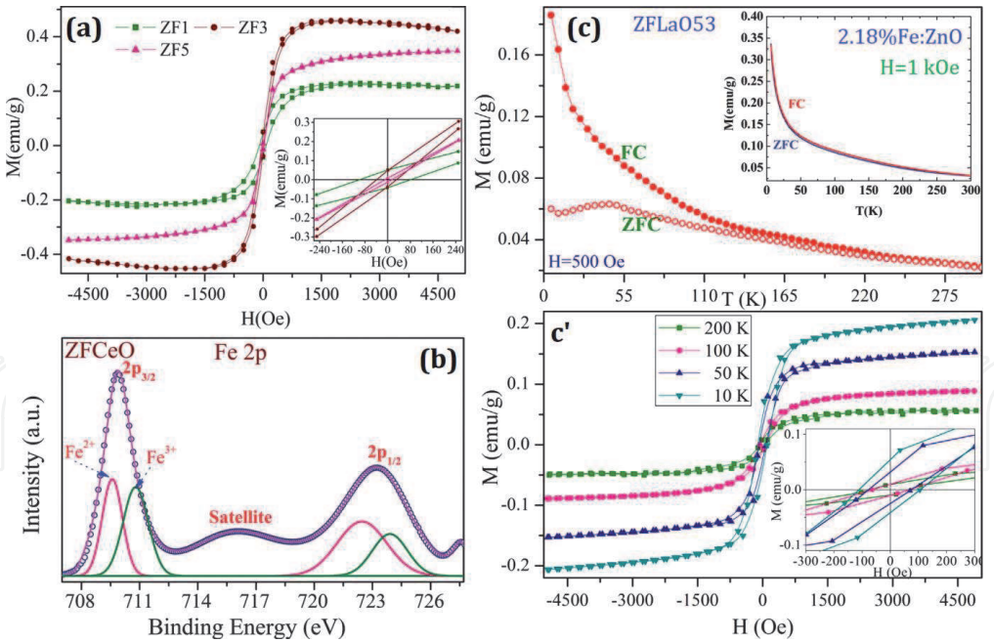

Figure 8.
(a) M-H hysteresis at room temperature for $Zn_{1-x}Fe_xO$ nanorods. (b) XPS spectrum of $Zn_{0.94}Fe_{0.03}Ce_{0.03}O$ nanostructures. (c) M(T) and (c′) M(H) for $Zn_{0.92}Fe_{0.05}La_{0.03}O$ nanoparticles (adapted from [21, 40, 50]).

like shape and size of nanostructures, concentration of dopants, and lattice defects. Furthermore, an F-center exchange (FCE) mechanism has been employed to illustrate the ferromagnetism of Fe-doped ZnO nanorods [51]. In this mechanism, the $Fe^{3+} - V_O^{2-} - Fe^{3+}$ group is common for which an electron is trapped in the oxygen vacancy to make an F-center, where the electron occupies an orbital (p_z), which overlaps the d_z^2 orbital of the *d* shells of both iron neighbors. The interactions between the ferromagnetic and paramagnetic or antiferromagnetic components lead to variations in saturation magnetization. Another mechanism is related with BMP formation by the alignment of the spins in TM ions [14].

3.6.2 Valence states of Fe in DMS ZnO influenced magnetic ordering

Figure 8b shows Fe 2p XPS spectra in a binding energy 707–728 eV of $Zn_{0.94}Fe_{0.03}Ce_{0.03}O$ (ZFCeO) nanoparticles to find their contribution into ferromagnetism [40]. The Fe^{2+} and Fe^{3+} $2p_{3/2}$ peaks always show satellite peaks at 6 and 8 eV above the principal peaks at 709.5 and 711.2 eV, respectively. The satellite peak is found in energy region of 6–8 eV above $2p_{3/2}$ principal peak, which indicates that ZFCeO DMS has Fe coexisting in both Fe^{2+} and Fe^{3+} states. For this, a multiple fitting of Fe 2p peaks with satellites show peaks corresponding to Fe^{2+} (709.60 and 722.51 eV) and Fe^{3+} (710.82 and 723.97 eV). It indicates that the Fe ions have mixed valences of +2 and + 3. The peaks related with $2p_{3/2}$ 709.89 eV and $2p_{1/2}$ 723.35 eV are also observed. Therefore, it is found that the Fe exists in mixed Fe^{2+} and Fe^{3+} oxidation states to give RTFM due to Fe^{2+}-Fe^{3+} transitions via oxygen vacancies.

3.6.3 Magnetic ordering with La ions in Fe/ZnO nanoparticles

The magnetic results for $Zn_{0.95}Fe_{0.05}O$ (ZFO5) and $Zn_{0.92}Fe_{0.05}La_{0.03}O$ (ZFLaO53) with M_s(emu g^{-1}) = 0.328 and 0.044 and M_r(emu g^{-1}) = 0.0083 and 0.0064 with H_c(Oe) = 12 and 144, respectively, are reported. The origin of observed magnetism at room temperature for La-doped ZFO5 is described via ZFC and FC magnetization SQUID measurement. **Figure 8c** shows temperature-dependent ZFC

and FC measurement with H = 500 Oe. The superimposition of ZFC/FC plots between 150 and 300 K, as well as their clear separation at low temperature with blocking temperature, T_B is observed. The observed T_B might correspond with Néel temperature, T_N (~42 K) of AF [52]. For more detail, M-H hysteresis is also measured at 200, 100, 50, and 10 K (**Figure 8c′**). The values M_s and M_r are enhanced with temperature when going from 300 to 10 K. This is due to the exchange interaction from AF to FM states. It is also shown that for 200–50 K, H_c varies so slowly, but at 10 K, it abruptly increased to 117 Oe, which is smaller than 144 Oe that is observed at room temperature. It means after AF transition, there is some possibility of FM clustered growth in ZFLaO sample [53]. The localization of electrons in magnetic clusters leads to develop high-spin and low-spin intersite electronic transitions. These magnetic clusters may also result from magnetic polarons [54].

3.7 DMS ZnO with Co, La, Gd, and Ce ions

3.7.1 RTFM in La- and Gd-doped $Zn_{0.95}Co_{0.05}O$ nanostructure

Figure 9a shows the M-H hysteresis for $Zn_{0.95}Co_{0.05}O$ (ZCO5), $Zn_{0.92}Co_{0.05}La_{0.03}O$ (ZCLO53), and $Zn_{0.92}Co_{0.05}Gd_{0.03}O$ (ZCGO53) nanostructure, measured at room temperature [36]. The pure ZCO5 shows weak ferromagnetism of M_s(emu g^{-1}) = 0.354 and M_r(emu g^{-1}) = 0.0276 with H_c(Oe) = 40 Oe. However, the La- and Gd-doped ZCO5 result into paramagnetic-type behavior. The weak ferromagnetism in ZCO5 exists due to antiferromagnetic, AF interactions among Co^{2+} ions [41, 55]. The AF coupling between Co impurities is favored when Co atoms are separated by more than a ZnO unit. While the ferromagnetic coupling is stable if AF interaction in neighboring Co–Co ions falling into contour of BMPs. However, the observed paramagnetism in La- and Gd-doped ZCO5 is related with

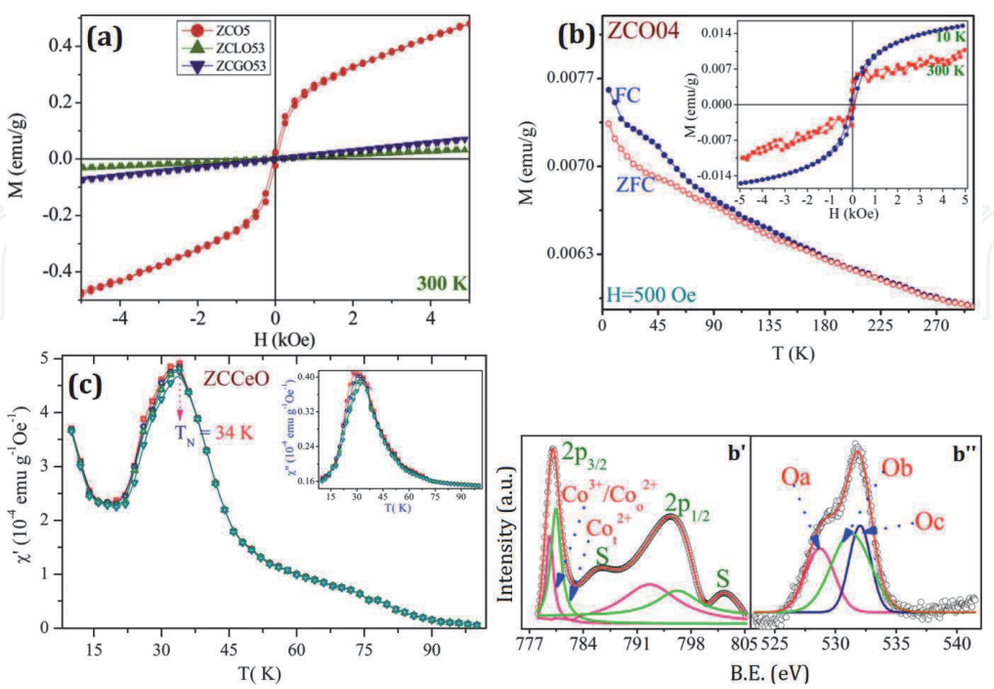

Figure 9.
(a) M-H hysteresis for Co-, La-, and Gd-doped ZnO nanoparticles, measured at room temperature. (b) M(T) and M(H) (inset) for $Zn_{0.996}Co_{0.004}O$ (ZCO04) nanoparticles. (b′ and b″) XPS spectra for Co 2p and O 1 s. (c) Temperature-dependent AC *magnetic susceptibility (χ) of ZFCeO nanoparticles (adopted from [15, 36, 40]).*

AF interaction establishment following 4f-5d-3d transition in Co and RE ions, suggested by Singh et al. [56].

3.7.2 Magnetic ordering in $Zn_{0.996}Co_{0.004}O$ nanoparticles

The $Zn_{0.996}Co_{0.004}O$ (ZCO04) nanoparticles synthesized with sol–gel process for which free-charge carriers and oxygen vacancies might induce long-range ferromagnetic ordering [15]. The XRD pattern results into wurtzite structure of ZCO04. The ZCO04 crystalline product has nanorod formation with D(nm) = 23 ± 3 and L(nm) = 57 ± 5. **Figure 9b** (inset) showed the RTFM of M_s (emu g^{-1}) 0.0062 and M_r (emu g^{-1}) = 0.0038 with H_c = 54 Oe. However, the pure ZnO nanorods are diamagnetic [50]. Xu et al. [57] reported RTFM with higher surface-to-volume ratio of nanostructure, which contribute large amount of surface oxygen vacancies defects. It is expected that the RTFM is attributed via exchange interactions among unpaired electron spins arising from either vacancies or surface defects, which is explained on the basis of donor impurity band exchange model form BMPs [58]. It is theoretically investigated that the oxygen vacancies have remarkable change in band structure of host oxides to induce ferromagnetism [59]. For this case of BMPs, the electrons are locally trapped by oxygen vacancies, with the trapped electron occupying an orbital overlapping with the *d* shells of Co neighbors.

To evaluate the origin of RTFM of ZCO04 nanoparticles, the temperature-dependent magnetization is given in **Figure 9b** via ZFC and FC at H = 500 Oe. The separation between ZFC and FC starts increasing with reducing temperature from 300 to 5 K which indicates antiferromagnetic interactions converted to ferromagnetic state. The absence of blocking temperature in ZFC might indicate long-range antiferromagnetism without any cluster growth. The exchange interactions between neighboring magnetic ions mediated by an F-center form a BMP contributing long-range ferromagnetism. At 10 K, the magnetic hysteresis is also shown in the inset of **Figure 9b** with M_s(emu g^{-1}) = 0.0154 and M_r(emu g^{-1}) = 0.002 with H_c(Oe) = 93.

3.7.3 Valence states of Co and O ions in $Zn_{0.996}Co_{0.004}O$ nanoparticles

Figures 9b′, b″ shows the XPS spectra for Co 2p and O 1 s of $Zn_{0.996}Co_{0.004}O$ (ZCO04) nanoparticles. For Co 2p, the doublet is the spin-orbit coupling ($2p_{3/2}$ and $2p_{1/2}$) given in **Figure 9b′**. The values of binding energy, Co $2p_{3/2} \sim 780.019$ eV, $2p_{1/2} \sim 795.51$ eV, and $\Delta E \sim 15.51$ eV, and satellite peak (S) ~ 785.48 eV are observed. The binding energies of Co $2p_{3/2}$ and $2p_{1/2}$ indicate that the Co ions exist either in +3 or + 2 valence states [60]. The difference ΔE of binding energy among Co $2p_{3/2}$ and $2p_{1/2}$ levels corresponds well with Co^{2+} that is homogeneously surrounded by oxygen in tetrahedral coordination [61]. However, the peak S is found in the energy region of 6–8 eV above the principle peak Co $2p_{3/2}$ and the value of S ~ 6 eV. It indicates the formation of multiple coordinations, i.e., tetrahedral or octahedral Co^{2+} ions. For more clarification, Co 2p peaks shown by octahedral Co^{2+} (Co_o^{2+}) and Co^{3+} and tetrahedral Co^{2+} (Co_t^{2+}) are clearly marked.

To find defects/vacancies in ZCO04, the O 1 s spectra is shown in **Figure 9b″**, which deconvoluted into three peaks (O_a, O_b, O_c) [15]. The peak located on low-binding energy side, $O_a \sim 528.79$ eV, is attributed with O^{2-} ions in wurtzite structure. This O_a of O 1 s is associated with Zn-O bonds. The O_b peak at 531.19 eV is associated with O^{2-} ions in the oxygen-deficient regions within the ZnO matrix, which indicate defect formation. The O_c peak at 532.16 eV is attributed to chemisorbed oxygen on the surface of the ZnO.

3.7.4 AC magnetic susceptibility (χ) of $Zn_{0.94}Fe_{0.03}Ce_{0.03}O$ nanoparticles

The temperature-dependent real, $\chi'(T)$, and imaginary, $\chi''(T)$, components of the AC magnetic susceptibility of Ce-doped ZFO nanoparticles at frequencies 100, 300, 500, and 1000 Hz are shown in **Figure 9c** [40]. The frequency-independent peak maxima of χ' correspond to magnetic phase transition into an AF state with T_N = 56 K is observed. A slight dispersion in the $\chi'(T)$ after the peak maxima is also observed. It indicates the existence of certain spin glass, ferromagnetic clusters and cluster glass magnetic type states [62]. However, the peak of $\chi''(T)$ increases with decreasing frequency. This is qualitatively different from the behavior of most spin glasses in which we expect an increase of the peak magnitude with increasing frequency. Thus, the obtained AC magnetization data supports the formation of the AF DMS materials with a certain cluster glass formation.

4. Conclusion

The spintronic materials are the ferromagnetic oxide semiconductors for which both charge and spin degrees of freedom exist, but with weak ferromagnetism and small coercivity, there is a limitation in practical applications. Thus, these DMSs are widely characterized for the development of semiconductor devices, which create a new dimensionality to control and achieve high T_C ferromagnetism. The first principle calculation revealed that the Cr, Fe, Co, and Ni dopants in ZnO prefer to occupy surface sites instead of bulk sites, while Mn exhibits no site preference and distributes uniformly in ZnO. In addition, the TM ions in ZnO are intrinsically AF because their substitution at Zn sites does not introduce any extra carriers. The interaction among localized spins on the TM ions and delocalized carrier electrons originating from the O vacancies is responsible for the required magnetic transition. The doping RE ions with intrinsic strong magnetic anisotropy and tailoring the coupling between dopants and defects should have a general approach toward a stable ferromagnetic order in DMS ZnO. The observed magnetism of DMS ZnO for both TM and RE ions might result with BMPs in oxygen vacancies.

Acknowledgements

This research work is financially supported by CSIR India, for giving a Senior Research Associate fellowship (Pool Scientist; letter No. B-12287).

Author details

Kuldeep Chand Verma[1,2]

1 Department of Physics, Panjab University, Chandigarh, India

2 CSIR-Central Scientific Instruments Organisation, Chandigarh, India

*Address all correspondence to: dkuldeep.physics@gmail.com

References

[1] Dietl T, Ohno H, Matsukura F, Cibert J, Ferrand D. Zener model description of ferromagnetism in zinc-blende magnetic semiconductors. Science. 2000;**287**: 1019-1022

[2] Furdyna JK. Diluted magnetic semiconductors. Journal of Applied Physics. 1988;**64**:R29-R56

[3] Chanda A, Gupta S, Vasundhara M, Joshi SR, Muttae GR, Singh J. Study of structural, optical and magnetic properties of cobalt doped ZnO nanorods. RSC Advances. 2017;**7**: 50527-50536

[4] Kittilstved KR, Liu WK, Gamelin DR. Electronic structure origins of polarity-dependent high-T_C ferromagnetism in oxide-diluted magnetic semiconductors. Nature Materials. 2006;**5**:290-297

[5] Sharma P, Gupta A, Rao KV, Owens FJ, Sharma R, Ahuja R, et al. Ferromagnetism above room temperature in bulk and transparent thin films of Mn-doped ZnO. Nature Materials. 2003;**2**:673-677

[6] Ohno H. A window on the future of spintronics. Nat. Mat. 2010;**9**:952-954

[7] Saitoh E. New order for magnetism. Nat. 2008;**455**:474-475

[8] Ohno H, Chiba D, Matsukura F, Omiya T, Abe E, Dietl T, et al. Electric-field control of ferromagnetism. Nature. 2000;**408**:944-946

[9] Chiba D, Yamanouchi M, Matsukura F, Ohno Electrical H. Manipulation of magnetization reversal in a ferromagnetic semiconductor. Science. 2003;**301**:943-945

[10] Dietl T. A ten-year perspective on dilute magnetic semiconductors and oxides. Nature Materials. 2010;**9**: 965-974

[11] Gupta JA, Knobel R, Samarth N, Awschalom DD. Ultrafast manipulation of electron spin coherence. Science. 2001;**292**:2458-2461

[12] Chambers S. Is it really intrinsic ferromagnetism? Nature Materials. 2010;**9**:956-957

[13] Kundaliya DC, Ogale SB, Lofland SE, Dhar S, Metting CJ, Shinde SR, et al. On the origin of high-temperature ferromagnetism in the low-temperature processed Mn-Zn-O system. Nature Materials. 2004;**3**: 709-714

[14] Coey JMD, Venkatesan M, Fitzgerald CB. Donor impurity band exchange in dilute ferromagnetic oxides. Nature Materials. 2005;**4**: 173-179

[15] Verma KC, Bhatia R, Kumar S, Kotnala RK. Vacancies driven magnetic ordering in ZnO nanoparticles due to low concentrated Co ions. Mater. Res. Exp. 2016;**3**:076103-076112

[16] Zhen WZ, Min ZJ, Gao HZ, Xiong LW. Effect of oxygen vacancy defect on the magnetic properties of Co-doped ZnO. Chinese Physics B. 2011;**20**: 027103

[17] Kumar V, Ntwaeaborwa OM, Soga T, Dutta V, Swart HC. Rare earth doped zinc oxide nanophosphor powder: A future material for solid state lighting and solar cells. ACS Photonics. 2017;**4**:2613-2637

[18] Venkatesan M, Fitzgerald CB, Lunney JG, Coey JMD. Anisotropic ferromagnetism in substituted zinc oxide. Physical Review Letters. 2004;**93**: 177206-14

[19] Wang Q, Sun Q, Jena P, Kawazoe Y. Magnetic properties of transition-metal-doped $Zn_{1-x}T_xO$ (T = Cr, Mn, Fe, Co,

and Ni) thin films with and without intrinsic defects: A density functional study. Physical Review B. 2009;**79**: 115407-115413

[20] Park YS, Litton CW, Collins TC, Reynolds DC. Exciton Spectrum of ZnO. Physics Review. 1966;**143**:512-519

[21] Verma KC, Kotnala RK. Oxygen vacancy induced by La and Fe into ZnO nanoparticles to modify ferromagnetic ordering. Journal of Solid State Chemistry. 2016;**237**:211-218

[22] Gao D, Zhang Z, Fu J, Xu Y, Qi J, Xue D. Room temperature ferromagnetism of pure ZnO nanoparticles. Journal of Applied Physics. 2009;**105**:113928-4

[23] Srinivasulu T, Saritha K, Ramakrishna Reddy KT. Synthesis and characterization of Fe-doped ZnO thin films deposited by chemical spray pyrolysis. Modern Elect. Mater. 2017;**3**: 76-85

[24] Tiwari N, Kumar S, Ghosh AK, Chatterjee S, Jhaa SN, Bhattacharyya D. Structural investigations of (Mn, Dy) co-doped ZnO nanocrystals using X-ray absorption studies. RSC Advances. 2017; **7**:56662-56675

[25] Valerio LR, Mamani NC, de Zevallos AO, Mesquita A, Bernardi MIB, Doriguetto AC, et al. Preparation and structural-optical characterization of dip-coated nanostructured Co-doped ZnO dilute magnetic oxide thin films. RSC Advances. 2017;**7**:20611

[26] Samanta A, Goswami MN, Mahapatra PK. Magnetic and electric properties of Ni-doped ZnO nanoparticles exhibit diluted magnetic semiconductor in nature. Journal of Alloys and Compounds. 2018;**730**: 399-407

[27] Verma KC, Kotnala RK. Understanding lattice defects to influence ferromagnetic order of ZnO nanoparticles by Ni, Cu, Ce ions. Journal of Solid State Chemistry. 2017;**246**: 150-159

[28] Wang D, Chen Q, Xing G, Yi J, Bakaul SR, Ding J, et al. Robust room-temperature ferromagnetism with Giant anisotropy in Nd-doped ZnO nanowire arrays. Nano Letters. 2012;**12**: 3994-4000

[29] Arora D, Asokan K, Mahajan A, Kaura H, Singh DP. Structural, optical and magnetic properties of Sm doped ZnO at dilute concentrations. RSC Advances. 2016;**6**:78122-78131

[30] Li H, Huang Y, Zhang Q, Qiao Y, Gu Y, Liu J. Facile synthesis of highly uniform Mn/Cocodoped ZnO nanowires: Optical, electrical, and magnetic properties. Nanoscale. 2011;**3**: 654-660

[31] Hou L, Zhou W, Zou B, Zhang Y, Han J, Yang X. Spin exciton interaction and related microphotoluminescence spectra of ZnSe:Mn DMS nanoribbon. Nanotechnology. 2017;**28**:105202-105211

[32] Midya N, Neogi SK, Ahmed Md A, Banerjee A, Kumar P, Kanjilald D. Correlation between magnetic and microstructural properties of low energy ion irradiated and un-irradiated $Zn_{0.95}Mn_{0.05}O$ films. RSC Advances. 2017;**7**:771-781

[33] Rouchdi M, Salmani E, Fares B, Hassanain N, Mzerd A. Synthesis and characteristics of Mg doped ZnO thin films: Experimental and ab-initio study. Results Phys. 2017;**7**:620-627

[34] Kaur J, Negi NS, Kotnala RK, Verma KC. Hydrothermal conditions on $Sn_{0.95}Co_{0.05}O_2$: Nanostructures, ferromagnetism and optical behavior. Journal of Sol-Gel Science and Technology. 2013;**65**:411-419

[35] Anjaneyulu C, Naresh G, Kumar VV, Tardio J, Rao TV, Venugopal A. Influence of rare earth

(La, Pr, Nd, Gd, and Sm) metals on the methane decomposition activity of Ni-Al catalysts. ACS Sustainable Chemistry & Engineering. 2015;**3**: 1298-1305

[36] Verma KC, Kotnala RK. Defects due to lattice distortion and nano-size intermediate ferromagnetism in La, Gd substituted. $Zn_{0.95}Co_{0.05}O$. Current Applied Physics. 2016;**16**: 175-182

[37] Sun LW, Shi HQ, Li WN, Xiao HM, Fu SY, Cao XZ, et al. Lanthanum-doped ZnO quantum dots with greatly enhanced fluorescent quantum yield. Journal of Materials Chemistry. 2012;**22**: 8221-8227

[38] Bantounas I, Singaravelu V, Roqan IS, Schwingenschlogl U. Structural and magnetic properties of Gd-doped ZnO. Journal of Materials Chemistry C. 2014;**2**:10331-10336

[39] Aravindh SA, Schwingenschloegl U, Roqan IS. Ferromagnetism in Gd doped ZnO nanowires: A first principles study. Journal of Applied Physics. 2014;**116**: 233906-5

[40] Verma KC, Kotnala RK. Defects-assisted ferromagnetism due to bound magnetic polarons in Ce into Fe, Co: ZnO nanoparticles and first-principle calculations. Physical Chemistry Chemical Physics. 2016;**18**:5647-5657

[41] Inamdar DY, Pathak AK, Dubenko I, Ali N, Mahamuni S. Room temperature ferromagnetism and photoluminescence of Fe doped ZnO Nanocrystals. Journal of Physical Chemistry C. 2011;**115**:23671-23676

[42] Vijayaprasath G, Murugan R, Mahalingam T, Hayakawa Y, Ravi G. Enhancement of ferromagnetic property in rare earth neodymium doped ZnO nanoparticles. Cer. Int. 2015;**41**: 10607-10615

[43] Ney V, Ye S, Kammermeier T, Ollefs K, Wilhelm F, Rogalev A, et al. Structural and magnetic analysis of epitaxial films of Gd-doped ZnO. Physical Review B. 2012;**85**: 235203-235207

[44] Chang LT, Wang CY, Tang J, Nie T, Jiang W, Chu CP, et al. Electric-field control of ferromagnetism in Mn-doped ZnO nanowires. Nano Letters. 2014;**14**: 1823-1829

[45] Ram M, Verma KC, Negi NS. Room temperature ferromagnetism and photoluminescence of nanocrystalline $Zn_{1-x}Co_xO$ thin films prepared by sol-gel MOD. Phil. Mag. Lett. 2014;**94**(7): 404-414

[46] Jin CG, Yang Y, Wu ZF, Zhuge LJ, Han Q, Wu XM, et al. Tunable ferromagnetic behavior in Cr doped ZnO nanorod arrays through defect engineering. Journal of Materials Chemistry C. 2014;**2**:2992-2997

[47] Wang Q, Sun Q, Chen G, Kawazoe Y, Jena P. Vacancy-induced magnetism in ZnO thin films and nanowires. Physical Review B. 2008;**77**: 205411

[48] Phan TL, Zhang YD, Yang DS, Nghia NX, Thanh TD, Yu SC. Defect-induced ferromagnetism in ZnO nanoparticles prepared by mechanical milling. Applied Physics Letters. 2013; **102**(7):072408

[49] Ney V, Ye S, Kammermeier T, Ney A, Zhou H, Fallert J, et al. Structural, magnetic, and optical properties of Co- and Gd-implanted ZnO(0001) substrates. Journal of Applied Physics. 2008;**104**:083904

[50] Kaur J, Kotnala RK, Gupta V, Verma KC. Anionic polymerization in Co and Fe doped ZnO: Nanorods, magnetism and photoactivity. Current Applied Physics. 2014;**14**:749-756

[51] Verma KC, Singh J, Ram M, Sharma DK, Sharma A, Kotnala RK. Enhancement in the magnetic, optical and electrical properties of $Ti_{0.97}Co_{0.03}O_2$ and $Ti_{0.97}Fe_{0.03}O_2$ nanoparticles with Ce co-doping. Physica Scripta. 2012;**86**:025704

[52] Fan JP, Li XL, Quan ZY, Xu XH. Tunable magnetic and transport properties of *p*-type ZnMnO films with *n*-type Ga, Cr, and Fe codopants. Applied Physics Letters. 2013;**102**: 102407-3

[53] Gnatchenko SL, Ratner AM, Baran M, Szymczak R, Szymczak H. Formation and interaction of ferromagnetic clusters in antiferromagnetic $YBa_2Cu_3O_{6+x}$ films. Physical Review B. 1997;**55**:3876-3885

[54] Kovaleva NN, Kugel KI, Bazhenov AV, Fursova TN, Loser W, Xu Y, et al. Formation of metallic magnetic clusters in a Kondo-lattice metal: Evidence from an optical study. Scientific Reports. 2012;**2**:890-897

[55] Walsh A, Da Silva JLF, Wei SH. Theoretical description of carrier mediated magnetism in cobalt doped ZnO. Physical Review Letters. 2008; **100**:256401-256404

[56] Singh SK, Rajaraman G. Decisive interactions that determine ferro/ antiferromagnetic coupling in {3d–4f} pairs: A case study on dinuclear {V(IV)-Gd(III)} complexes. Dalton Transactions. 2013;**42**:3623-3630

[57] Xu X, Xu C, Dai J, Hu J, Li F, Zhang S. Size dependence of defect-induced room temperature ferromagnetism in undoped ZnO nanoparticles. Journal of Physical Chemistry C. 2012;**116**:8813-8818

[58] Banerjee S, Mandal M, Gayathri N, Sardar M, et al. Applied Physics Letters. 2007;**91**:182501

[59] Hsu HS, Huang JCA, Huang YH, Liao YF, Lin MZ, Lee CH, et al. Evidence of oxygen vacancy enhanced room-temperature ferromagnetism in Co-doped ZnO. Applied Physics Letters. 2006;**88**:242507

[60] Lu XF, Wu DJ, Li RZ, Li Q, Ye SH, Tong YX, et al. Hierarchical $NiCo_2O_4$ nanosheets@hollow microrod arrays for high-performance asymmetric supercapacitors. Journal of Materials Chemistry A. 2014;**2**:4706-4713

[61] Lee HJ, Jeong SY, Cho CR, Park CH. Study of diluted magnetic semiconductor: Co-doped ZnO. Applied Physics Letters. 2002;**81**:4020

[62] Rathore SS, Vitta S. Effect of divalent Ba cation substitution with Sr on coupled 'multiglass' state in the magnetoelectric multiferroic compound $Ba_3NbFe_3Si_2O_{14}$. Scientific Reports. 2015;**5**:9751